

# Exploiting Synchronization Properties of Correlated Electron Devices in a Non-Boolean Computing Fabric for Template Matching

Abhinav Parihar, Nikhil Shukla, Suman Datta, *Fellow, IEEE*, and Arijit Raychowdhury, *Senior Member, IEEE*

**Abstract**—As complementary metal–oxide–semiconductor (CMOS) scaling continues to offer insurmountable challenges, questions about the performance capabilities of Boolean, digital machine based on Von-Neumann architecture, when operated within a power budget, have also surfaced. Research has started in earnest to identify alternative computing paradigms that provide orders of magnitude improvement in power-performance for specific tasks such as graph traversal, image recognition, template matching, and so on. Further, post-CMOS device technologies have emerged that realize computing elements which are neither CMOS replacements nor suited to work as a binary switch. In this paper, we present the realization of coupled and scalable relaxation-oscillators utilizing the metal–insulator–metal transition of vanadium-dioxide (VO<sub>2</sub>) thin films. We demonstrate the potential use of such a system in a non-Boolean computing paradigm and demonstrate pattern recognition, as one possible application using such a system.

**Index Terms**—Correlated electron systems, coupled relaxation oscillators, Non-Boolean computation, template matching.

## I. INTRODUCTION

COMPLEMENTARY metal–oxide–semiconductor (CMOS) transistor scaling has been the cornerstone of the computational industry since the invention of the integrated circuit and has led to unprecedented level of integration with billions of high-speed nano-transistors on a single chip reducing cost per function. However, beyond the 3 nm technology node, conventional CMOS transistor scaling will slow down significantly not only due to intrinsic transistor channel length scaling limitation due to direct source to drain tunneling leakage, but also due to overwhelming adverse impact of parasitic

resistance and capacitance associated with source/drain contact as well as interconnect. Thus, a transformative approach is required to explore nonconventional devices beyond the CMOS technology as well as unconventional computational paradigms [1]–[4]. In the last few years, nano-oscillator based computing paradigms have gained popularity, particularly spin torque oscillator (STO) based coupled systems [5]–[9]. Also systems of complex oxides capable of performing spontaneous metal–insulator–metal transitions have generated interest in their applicability in realizing systems of coupled nano-oscillators. In this paper, we demonstrate the collective dynamics of carriers in a correlated material (Vanadium dioxide) and investigate a non-Boolean information processing architecture, which fundamentally embraces “let physics do the computing” paradigm. Through experimental demonstration we show that Vanadium dioxide (VO<sub>2</sub>) reveals strong collective carrier dynamics that can enable novel functional devices and architectures for brain-inspired neuro-morphic computation. In particular, the synchronization and coupling dynamics of VO<sub>2</sub> based relaxation oscillators is investigated. Vanadium dioxide (VO<sub>2</sub>) undergoes a first-order insulator–metal phase transition marked by an abrupt change in conductivity up to five decades in magnitude. By electrically accessing and stabilizing a regime characterized by the coexistence of competing metallic and insulating phases in the vicinity of the insulator–metal transition, we demonstrate compact, scalable, inductor-less and functionally dense relaxation oscillators capable of multi-GHz performance when integrated on-die. We explore the synchronization dynamics of such oscillators, using long-range electrical coupling; and through experiments and models we present frequency locking as well as phase synchronization in pairwise coupled oscillators. As a demonstration of the computational capability of such a fabric, template matching is performed and low rates of “false accept” and “false reject” across large image databases is noted. We further present the role of mismatch and variation in this computing paradigm.

## II. VO<sub>2</sub> OSCILLATOR CIRCUIT AND DEVICE FABRICATION

Transition metal oxides exhibit unique properties like metal–insulator transitions [10], colossal magnetoresistance [11], magnetism [12], and superconductivity [13] some of which are particularly interesting for electronic applications. One such material that has been of particular interest is vanadium dioxide (VO<sub>2</sub>). VO<sub>2</sub> is a correlated electron material system that undergoes metal-insulator transition, usually just

Manuscript received April 06, 2014; revised July 24, 2014; accepted September 17, 2014. Date of publication October 17, 2014; date of current version December 09, 2014. The work of N. Shukla and S. Datta was supported by the Office of Naval Research under Award N00014-11-1-0665. The work of S. Datta was also supported by the National Science Foundation (NSF) Expeditions in Computing Award 1317560. The work of A. Parihar and A. Raychowdhury was supported by Intel Corporation. This paper was recommended by Guest Editor H. Hunter.

A. Parihar and A. Raychowdhury are with the School of Electrical and Computer Engineering, Georgia Institute of Technology, Atlanta, GA 30332 USA (e-mail: aparihar6@gatech.edu; arijit.raychowdhury@ece.gatech.edu).

N. Shukla and S. Datta are with the Electrical Engineering Department, The Pennsylvania State University, University Park, PA 16802 USA (e-mail: nss152@psu.edu; sdatta@engr.psu.edu).

Color versions of one or more of the figures in this paper are available online at <http://ieeexplore.ieee.org>.

Digital Object Identifier 10.1109/JETCAS.2014.2361069

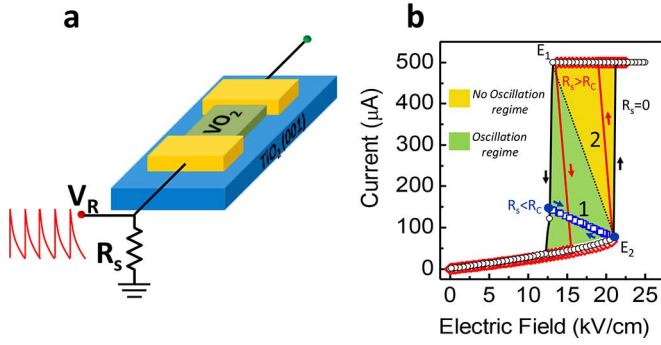


Fig. 1. (a) Schematic of the circuit used to access the nonhysteretic transition regime in VO<sub>2</sub> via negative feedback generated by the series resistor  $R_S$ . Electric field across VO<sub>2</sub>  $E = (V_{in} - V_R)/L_{VO2}$  plays a crucial role in the phase transition. (b) Current-electric field characteristics across VO<sub>2</sub> for different  $R_S$ . External resistance  $R_S$  modifies the VO<sub>2</sub> phase transition dynamics through negative feedback. An oscillation regime can be accessed using the appropriate  $R_S$  ( $> R_C$ ). Electrical load lines for oscillatory (1) and nonoscillatory (2) regime are superimposed.

above room temperature ( $\sim 340$  K). This phase transition is usually associated with a large and abrupt change in conductivity up to five orders in magnitude [14] along with a structural change (monoclinic M1 in insulating state; rutile in metallic phase). The exact physics of the phase transition is a subject of debate with the principle theories being the Mott–Hubbard transition and Peierls transition with some researchers suggesting a weighted contribution from both mechanisms. However in the recent times, the research paradigm into this material has evolved from pure academic curiosity to pursuit of real-world devices like MOTT FETs [15], sensors [16] and various electronic components. This is because in addition to the large and abrupt change in conductivity, it has been shown that such a phase transition can not only be triggered using various external stimuli including thermal [17], electrical [18], [19], optical [20], and strain (mechanical) [21] but can also occur on a femto-second time scale [20]. In this paper, we exploit the large conductivity change associated with the phase transition to realize scalable relaxation oscillators. The VO<sub>2</sub> oscillator circuit consists of a two terminal VO<sub>2</sub> device in series with a resistor  $R_S$ , as shown in Fig. 1(a). The role of the  $R_S$  will be explained in the coming sections of the paper. The VO<sub>2</sub> two terminal devices are fabricated on 17.7-nm ultrathin VO<sub>2</sub> films. The VO<sub>2</sub> films are epitaxially grown on a TiO<sub>2</sub> (001) substrate employing reactive oxide molecular-beam epitaxy [22]. Due to epitaxial mismatch, the VO<sub>2</sub> films are biaxially strained in compression by  $-0.9\%$ . The compressive strain reduces the phase transition temperature of VO<sub>2</sub> from 340 K to  $\sim 310$  K. First, the electrodes are patterned using contact lithography followed by electron beam evaporation of metal electrodes. Next the channel width and isolation are defined by electron beam lithography followed by a halogen based dry etch. Unless stated otherwise, all electrical measurements reported are performed near room temperature ( $18^\circ\text{C}$ ). The relatively simple device structure and fabrication flow will allow for easier device scaling and high packing density for such devices.

### III. OPERATING PRINCIPLE OF VO<sub>2</sub> OSCILLATORS

The electrically driven phase transition in VO<sub>2</sub> is abrupt, however it usually comes at the cost of hysteresis. The VO<sub>2</sub> oscillators harness this abrupt and hysteretic electrically driven change in conductivity of VO<sub>2</sub> to realize oscillations. The VO<sub>2</sub> oscillators can be realized at temperature when the VO<sub>2</sub> is nominally in the insulating state. When electrically driven across the phase transition (with  $R_S = 0\ \Omega$ ) the insulator-to-metal transition (IMT) and the metal-to-insulator transition (MIT) occur at different critical fields  $E_2$  and  $E_1$ , respectively. These critical fields are determined by the physics of the electrically driven phase transition (the exact mechanism of this phase transition is also being debated). However, these fields can be experimentally determined and without loss of generality it can be concluded that  $E_2$  represents the critical point after which high conductivity metallic phase is electrically stabilized while  $E_1$  is the critical point at which the metallic phase can no longer be electrically stabilized and the device returns to its high resistivity insulating state.

In contrast to this hysteretic transition, a nonhysteretic transition can be induced by modifying the phase transition dynamics so that triggering the IMT (by surpassing  $E_2$ ) results in a negative differential resistance (NDR) characterized by an increase in conductivity as well as a simultaneous reduction in electric field across the VO<sub>2</sub> device. If the field across the VO<sub>2</sub> now drops below the critical field  $E_1$ , it makes the high conductivity metallic phase unstable resulting in a spontaneous MIT. Representing this scenario through an electrical load line [Fig. 1(b)], a VO<sub>2</sub> device operating on load line “1” will undergo a nonhysteretic transition, whereas a device operating on load line “2” will go through a hysteretic transition.

While the NDR and the load lines described above cannot be achieved using the  $R_S = 0\ \Omega$  configuration, the addition of a simple  $R_S = 0\ \Omega$  in series makes this feasible.  $R_S$  provides a stabilizing negative feedback compensating the positive internal feedback arising from the collective carrier dynamics as the VO<sub>2</sub> undergoes phase transition. This negative feedback modulates the current-electric field characteristics across the VO<sub>2</sub> and establishes the load line relation

$$E_{VO2} = E_2 - \frac{\Delta I_{VO2} R_S}{L_{VO2}} \quad (1)$$

where  $\Delta I_{VO2} = I_{VO2}(E_{VO2}) - I_{VO2}(E_2)$  and  $L_{VO2}$  is the VO<sub>2</sub> channel length. From (1), it is evident that  $R_S$  tunes the VO<sub>2</sub> current-electric field characteristics and sets the criteria for nonhysteretic/hysteretic switching. The critical resistance  $R_C$  that enables the nonhysteretic regime of operation ensures that the metallic phase is never completely stabilized and is given by

$$R_C \geq \frac{L_{VO2}}{W_{VO2} t_{VO2}} \left| \frac{E_2 - E_1}{\sigma_{SC} E_2 - \sigma_m E_1} \right| \quad (2)$$

where  $W_{VO2}$  and  $t_{VO2}$  are the VO<sub>2</sub> channel width and thickness, respectively, and  $\sigma_m$  and  $\sigma_{sc}$  are the equivalent insulating and metallic state conductivities, respectively.

Further, the conductivity in the NDR regime as indicated by  $\Delta I_{VO2}$  is tuned by the electric field (1) with conductivity increasing as the electric field drops (and vice-versa). Such a system will oscillate if the conductivity and the electric-field

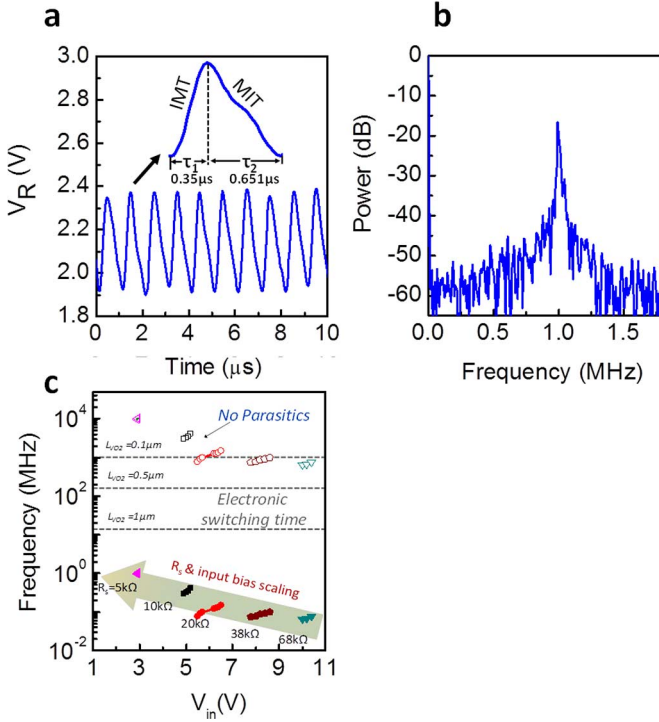


Fig. 2. (a) Measured time domain waveform of the VO<sub>2</sub> relaxation oscillator (Inset) shows the waveform for one oscillation period with the two time constants ( $\tau_1$  and  $\tau_2$ ) associated with IMT and MIT.  $\tau_2$  ( $=0.651 \mu\text{s}$ ) is larger than  $\tau_1$  ( $=0.35 \mu\text{s}$ ). (b) Power spectrum (power expressed as mean square amplitude in dB) of the oscillator. (c) Frequency scaling of the VO<sub>2</sub> relaxation oscillator. The frequency increases as the external  $R_s$  is scaled down. Device resistance has also been scaled to further increase the output frequency. Hollow symbols project the effect of eliminating parasitic elements. The dimension dependent electronic time constants (grey lines) will ultimately limit  $f_{\text{osc}}$ .

across the device modulate each other in a way that the field driven restoring force enables the system to trace the same electrical trajectory periodically. This criterion is fulfilled only in the nonhysteretic operating regime and results in sustained oscillations when  $R_s > R_c$ . Hence, harnessing the correlated physics in VO<sub>2</sub> using appropriate circuit elements allows us to realize relaxation oscillations in VO<sub>2</sub>. It must be noted that the negative feedback required to stabilize the oscillations in VO<sub>2</sub> need not necessarily be provided through a resistor  $R_s$  only. Such a feedback can also be realized by substituting the resistor with a MOSFET which can provide better oscillator functionality as discussed in the following sections.

The measured time domain waveform of the VO<sub>2</sub> oscillator (Fig. 2(a); single time period shown as inset) shows an exponential voltage buildup and decay (across  $R_s$ ) associated with MIT and IMT in VO<sub>2</sub> respectively and is characterized by two  $R$ - $C$  time constants  $\tau_1$  and  $\tau_2$  [see inset Fig. 2(a)] which primarily control the oscillation frequency.  $\tau_1$  ( $=0.35 \mu\text{s}$ ), associated with the IMT is smaller than  $\tau_2$  ( $=0.65 \mu\text{s}$ ). The corresponding power spectrum for the oscillations is shown in Fig. 2(b). The exponential nature of the time domain waveform results in a gradual decay of the frequency harmonics and therefore the first harmonic is only  $\sim 10$  dB below the fundamental frequency (not shown here). The power distribution in the harmonics may be altered using a voltage controlled external resistance.

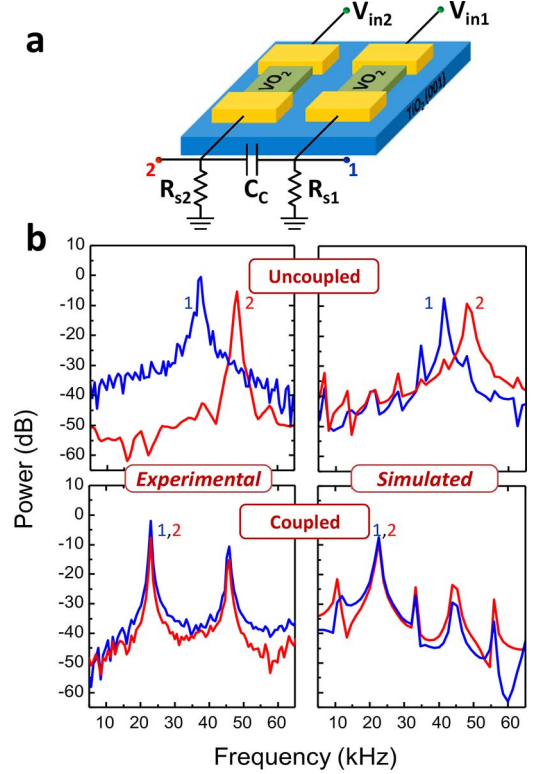


Fig. 3. (a) Schematic of two capacitively coupled VO<sub>2</sub> oscillators tuned to different oscillating frequencies with  $R_{s1} = 38 \text{ k}\Omega$  ( $=6R_c$ ) and  $R_{s2} = 47 \text{ k}\Omega$  ( $=7.5R_c$ ). (b) Experimental and simulated power spectrum (power expressed as mean square amplitude in dB) of both oscillators before and after coupling. Individual oscillator frequencies lock to a new frequency when coupled capacitively ( $C_c = 680 \text{ pF}$ ).

Further, we study the oscillator frequency ( $f_{\text{osc}}$ ) and dimensional scalability which is crucial to implementing dense, large scale VO<sub>2</sub> oscillator circuits. Since  $f_{\text{osc}}$  is set by the  $RC$  time constant of the oscillator circuit, we explore  $f_{\text{osc}}$  scaling with  $R_s$  [Fig. 2(c)]. As  $R_s$  is reduced, frequencies up to 1 MHz are experimentally realized. The  $R$ - $C$  time constants  $\tau_1 = 0.35 \mu\text{s}$  and  $\tau_2 = 0.35 \mu\text{s}$  for the  $f_{\text{osc}} = 1 \text{ MHz}$  case are much larger than the intrinsic electronic switching time [23] associated with the phase transition in VO<sub>2</sub> and therefore there is ample scope for device and frequency scaling. All experiments in this work are performed using discrete components (resistors) and eliminating the parasitic elements associated with the present wiring schemes through monolithic integration as well as device scaling [24] will increase  $f_{\text{osc}}$ .

#### IV. EXPERIMENTAL DEMONSTRATION OF COUPLED VO<sub>2</sub> OSCILLATORS

The realization of compact, inductor-free nonlinear oscillators in the VO<sub>2</sub> material system that use charge as the fundamental state variable portends the exploration of the coupling dynamics of such oscillators, a crucial step towards realization of non-Boolean computing architectures. Long range electrical charge based coupling is crucial to implementing large oscillator arrays compared to other state-variables (like spin), which may have limited coherence length at room temperature.

Fig. 3(a) shows a schematic of the coupled oscillator circuit. Prior to coupling, the two individual VO<sub>2</sub> oscillators frequencies are,  $f_{\text{osc},1} = 48.43 \text{ kHz}$  and  $f_{\text{osc},2} = 37.27 \text{ kHz}$  [Fig. 3(b)], which are set by using appropriate  $R_s$  values:  $R_{s1} = 38 \text{ k}\Omega$

( $6R_c$ ) and  $R_{s2} = 47 \text{ k}\Omega$  ( $7.5R_c$ ). After the oscillators are capacitively coupled ( $C_C = 680 \text{ pF}$ ) they frequency lock and converge to a single resonant frequency (22.95 kHz). This is accompanied by a sharp narrowing of the spectral line width [Fig. 3(b)]. The reduced line-width after locking reflects the mutual feedback induced stabilization against noise [25], implying that the synchronized state is a highly stable configuration for the coupled system. Simulations were performed on coupled differential equations for the circuit assuming capacitive charging and discharging for the MIT device. Detailed explanation of the model and the system dynamics is discussed in Section V. It can be noted in Fig. 3(b) that a close match exists between experimental and simulation results in the PSD before and after coupling.

The use of capacitive coupling is motivated by the high pass filtering characteristics of the coupling configuration, which ensures that the individual oscillators can synchronize without mutually affecting their dc quiescent point.  $C_C$  modifies the frequency dynamics of each oscillator through an effective coupling term  $C_{\text{eff}}$

$$C_{\text{eff}} = C_C C_1 + C_C C_2 + C_1 C_2 \quad (3)$$

where  $C_1$  and  $C_2$  are the net capacitances of each oscillator.  $C_1$  and  $C_2$  include the internal domain capacitances associated with each  $\text{VO}_2$  film and device as well the parasitic elements. The  $C_C$  element stores and dynamically redistributes reactive (nondissipative) power between the oscillators facilitating synchronization.

## V. COMPARISON WITH OTHER OSCILLATORS

Most of the work in oscillators till now have focussed on high frequency and high power output for microwave source generation to reach THz frequency benchmarks. These include fundamental sources like Gunn devices and RTDs as well as frequency multipliers [26]. Work in these devices have not investigated the dynamical properties of coupled oscillatory systems or their potential applications in computation. For computation, PLL-based systems were proposed [27] but these suffer from nonscalability both in process and voltage, high power requirements, and complex nontrivial coupling mechanisms. Spin torque oscillators (STOs) [28] were developed for high frequencies and RF applications which motivated work on coupled STO systems and their phase properties [2] as well. But these devices, although very competitive in scalability and process integration, have high bias current requirements ( $\sim 8 \text{ mA}$  compared to  $10\text{--}50 \text{ }\mu\text{A}$  in  $\text{VO}_2$  devices [25]). In this paper, we endeavor to control the phase dynamics of  $\text{VO}_2$  based coupled oscillators and apply such dynamics in solving computationally hard problems. In particular, template matching has been chosen as the application platform.  $\text{VO}_2$  based oscillators provide a viable alternative to other nano-scaled oscillator technologies as they are not only compact but also have low voltage and power requirements. For instance, the switching electric fields in IMT/MIT processes are small, around  $10\text{--}50 \text{ KV/cm}$ , compared to  $1\text{--}5 \text{ MV/cm}$  zener fields in inter-band tunneling NDR oscillators. However, since they are based on relaxation oscillations, their isolated dynamics, coupling mechanisms and coupling dynamics provide additional challenges in analysis, modeling and implementation.

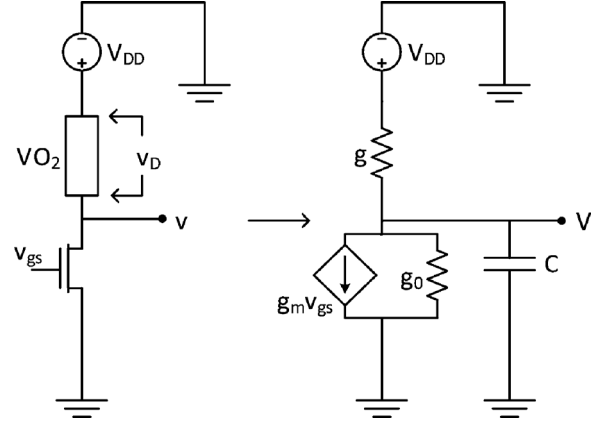


Fig. 4.  $\text{VO}_2$  oscillator with series transistor and its equivalent circuit. Transistor is replaced by its small signal equivalent and the MIT device is modeled as charging of a capacitor through a conductance which depends on the phase of the device at that time instant.

## VI. RELAXATION OSCILLATOR—THEORETICAL ANALYSIS

### A. Single Oscillator

The experimental demonstration of a  $\text{VO}_2$  based relaxation oscillator and its coupling dynamics motivate the investigation of a programmable system of coupled oscillators whose frequency of coupling, coupling dynamics and phase relations can be controlled. One way to do so, is to replace the passive resistor in series with the  $\text{VO}_2$  device with an active element, e.g., a MOSFET whose gate voltage would modulate the effective series resistance and hence the locking and synchronization dynamics of the coupled system. In this section, we demonstrate such a system and show through analytical and numerical models the dynamical properties of such a system.

As has already been mentioned, the relaxation oscillators we consider consist of a phase change material  $\text{VO}_2$  in series with a resistive device, which in our case is a transistor so that the frequency of oscillations can be controlled by the gate voltage of the transistor. We model this system in terms of charging and discharging of a capacitor through the device resistance and the MOSFET series resistance, respectively [29] (Fig. 4). The MOSFET operates in its saturation region and is modeled using a voltage controlled current source and an output impedance. The transition voltages for changing the state of the device from insulating to metallic and vice versa correspond to voltages  $v_l$  and  $v_h$  respectively at the output node. These voltages correspond to the critical electric fields ( $E_1$  and  $E_2$ ) that cause phase transition in the  $\text{VO}_2$  device. Let the following parameters be defined for the phase change device:  $g_{di}$ —internal conductance of device in insulating phase,  $g_{dm}$ —internal conductance of device in metallic phase,  $g_m$ —trans-conductance of series transistor,  $g_0$ —output conductance of series transistor, and  $c$ —internal capacitance of device. For simplicity, all voltages in the system are normalized to  $v_{dd}$  (including  $v_l$ ,  $v_h$  and  $v_{gs}$  applied at the transistor gates); hence,  $v_{dd} = 1$ . When  $g_{di} \ll g_0$  and  $g_{dm} \gg g_0$ , the equation for the system can be simplified to

$$cv' = -g(s)v + p(s) \quad (4)$$



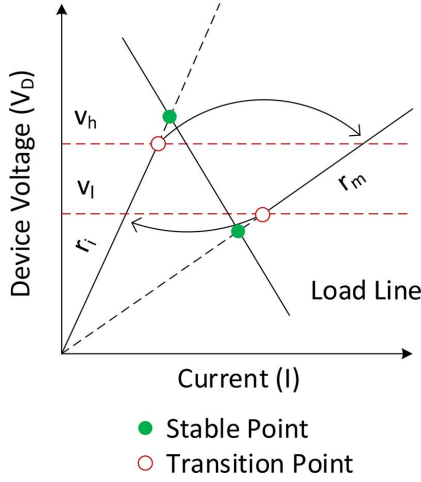


Fig. 5. Phase space of a VO<sub>2</sub> device with load line for a resistive load connected in series. Two lines with slopes  $r_i$  and  $r_m$  show the region of operation of device in insulating and metallic phase, respectively. Intersection points of these lines with the load line are the stable points. Stable points should lie outside the region bounded by the transition points (shown by dashed lines) for sustained oscillations.

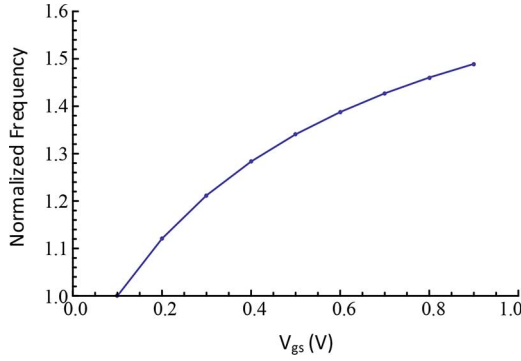


Fig. 6. Frequency of VO<sub>2</sub> oscillator (normalized to frequency at  $v_{gs} = 0.1$ ) as a function of gate voltage.

where  $s$  denotes the phase of the device (0 for metallic, and 1 for insulating) and  $g(s)$  and  $p(s)$  depend on the device phase  $s$  as follows:

$$\begin{aligned} g(s) &= \begin{cases} g_{dm}, & s = 0 \\ g_0, & s = 1 \end{cases} \\ p(s) &= \begin{cases} g_{dm}, & s = 0 \\ -g_m v_{gs}, & s = 1 \end{cases} \end{aligned} \quad (5)$$

The conditions for oscillation can be explained using the phase diagram of the MIT device (Fig. 5) [30]. Lines with slopes  $r_i$  and  $r_m$  are the region of operation of the device in insulating and metallic states respectively. When a MOSFET is connected in series, intersections of these regions with the load line would determine the stable points. For sustained oscillations, the stable points should lie outside the region bounded by the transition points on V axis. This ensures that the system would never reach a stable point as it will encounter a transition before reaching one, but will constantly be pulled by one of the stable points and hence gives rise to oscillations. Fig. 6 illustrates the frequency control of the relaxation oscillator with  $v_{gs}$  and illustrates the capability of the MOSFET to control the oscillation dynamics.

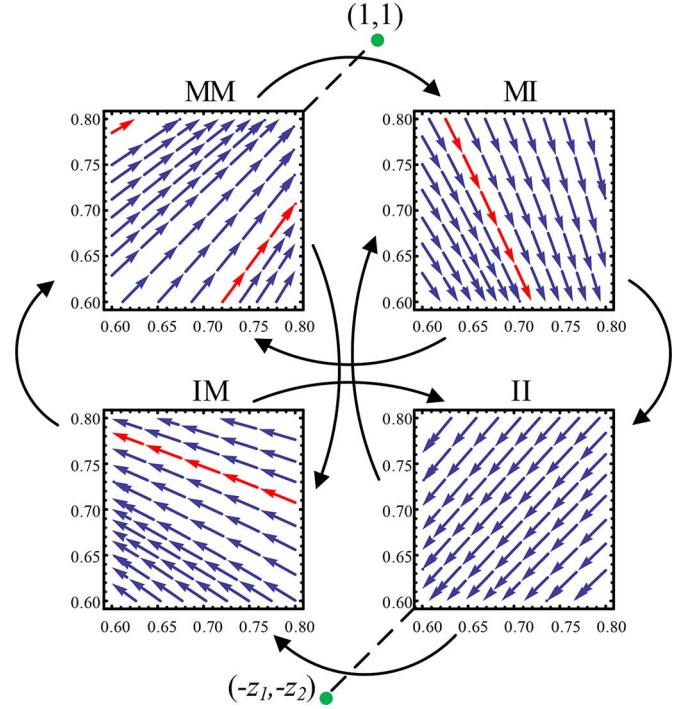


Fig. 7. Regions of state space of the coupled system with parameter values  $g : g_0 : g_m = 3 : 1 : 3$ ,  $\alpha = 10$ ,  $v_{gs1} = 0.5$  and  $v_{gs2} = 0.4$ . Fixed points in states MM and II are shown where  $z_1 = g_{m1} v_{gs1}$  and  $z_2 = g_{m2} v_{gs2}$ . Steady state periodic orbit of the system is marked in red among the flows in the state space. Arrows outside the state space show the transitions between the regions when the system hits any edge.

### B. Coupled Systems and Synchronization

When two such relaxation oscillators are coupled electrically, their phase dynamics would evolve over time till a steady state is reached. Such synchronization is well known in coupled networks of oscillators [31]. The system we consider consists of two relaxation oscillators that are coupled using a capacitor  $c_c$ . The equation of the system of coupled oscillators is given by

$$c_c \begin{bmatrix} \alpha_1 + 1 & -1 \\ -1 & \alpha_2 + 1 \end{bmatrix} \begin{bmatrix} v'_1 \\ v'_2 \end{bmatrix} = \begin{bmatrix} -g_1(s_1)v_1 \\ -g_2(s_2)v_2 \end{bmatrix} + \begin{bmatrix} p_1(s_1) \\ p_2(s_2) \end{bmatrix} \quad (6)$$

where  $g_i(s_i)$  and  $p_i(s_i)$  are as defined above for each oscillator and  $\alpha$  is the ratio  $(c_1)/(c_c) = (c_2)/(c_c)$ . We start by defining the state space of the coupled system. At any time, the state of the system is characterized by  $(v_1, v_2, s_1, s_2)$ .  $s_1$  and  $s_2$  take only two values each—0 and 1, as explained before, and  $v_1$  and  $v_2$  vary between  $v_l$  and  $v_h$ . Hence, we can represent the state space as four regions of 2-D state spaces corresponding to four combinations of phases of the two devices—MM (metallic–metallic), MI (metallic–insulating), IM (insulating–metallic), and II (insulating–insulating) (Fig. 7). It is assumed that the parameters are varied in a way that the flows in all the states remain monotonic in the direction as shown. This monotonicity condition guarantees oscillations of both oscillators in steady state and can be considered as an extension of the previous condition for oscillation in case of a single oscillator. As the flow is linear in all the four regions of the state space, there is a single fixed point in all states. The fixed points for regions MM and II are shown in

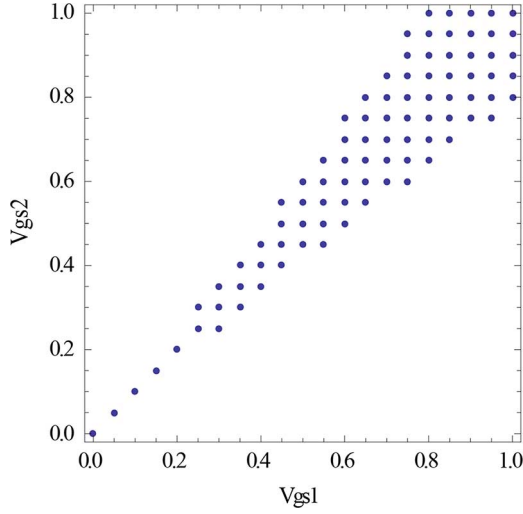


Fig. 8. Region in the  $(v_{gs1}, v_{gs2})$  plane for which the coupled system locks. Locking range is larger for larger  $v_{gs}$  values.

Fig. 7. Due to symmetry in region MM, if the system starts from bottom left corner, it ends in the opposite corner and the flow is symmetric along the diagonal line as shown. Such symmetry is possible in state II only when  $v_{gs1} = v_{gs2}$ .

### C. Locking and Stable Orbits

A VO<sub>2</sub> oscillator with a series transistor can be considered as a voltage controlled oscillator, with the gate voltage controlling its frequency of oscillation. When two such oscillators are coupled, the system is expected to lock for closer frequencies, and for identical oscillators, closer frequencies correspond to close values of  $v_{gs}$ . The mechanism of locking, however, is different from the mechanism by which coupled sinusoidal oscillators lock. The locking range in terms of  $v_{gs}$ , i.e., the range of  $v_{gs}$  for which the system locks and settles to a stable periodic orbit in steady state, is depicted in Fig. 8. Locking is determined by monitoring the waveforms of both oscillators to see if the time difference in their successive peak values become constant after a while or not. The locking range of Fig. 8 describes the region of a single rational rotation number and the region outside describes irrational or other rational rotation numbers [29]. The steady state periodic orbits of the coupled system for  $v_{gs1} = 0.3$  and varying  $v_{gs2}$  are shown in Fig. 9. As can be seen, the system has a butterfly shaped stable orbit when  $v_{gs}$  values are close, which transitions into a rectangular orbit as  $v_{gs}$  values diverge and finally the system ceases to lock after a certain point. The symmetric butterfly curve is along the diagonal that corresponds to out-of-phase oscillation of the oscillators in time domain. As the system moves away from symmetry, the phase difference between the oscillators in time domain reduces but breaks synchronization much before reaching in-phase locking state.

## VII. RELAXATION COMPARATOR

The trajectories in the phase space can be used to capture the difference in the values of  $v_{gs1}$  and  $v_{gs2}$  using an averaged XOR measure on the output waveforms. The averaged XOR measure is defined as first thresholding the output to binary values, second applying XOR operation on these binary values at every

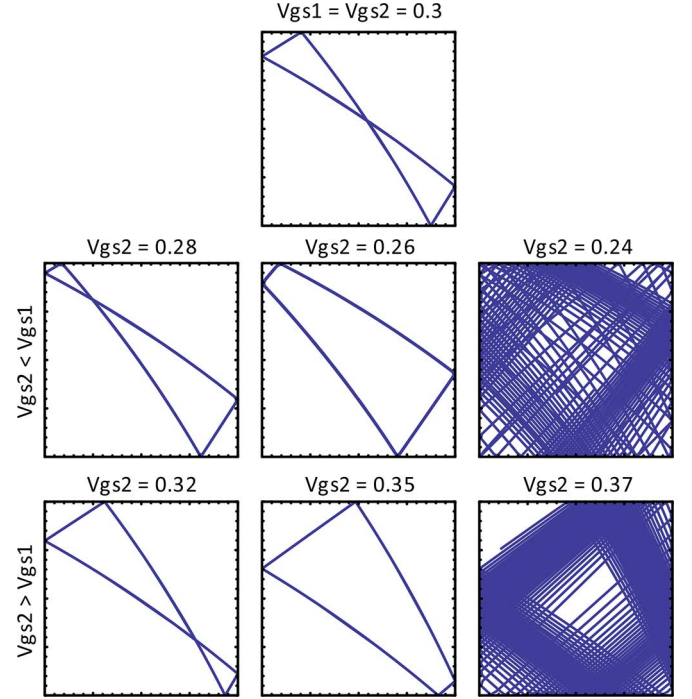


Fig. 9. Steady state orbits in the state space of the coupled system for fixed  $v_{gs1} = 0.3$  and varying  $v_{gs2}$ . When the both  $v_{gs}$  values are equal, the stable periodic orbit is butterfly shaped along the diagonal that correspond to out-of-phase locking. As the difference in the  $v_{gs}$  values increase, the periodic orbit slowly changes to rectangular and finally breaks synchronization after a point.

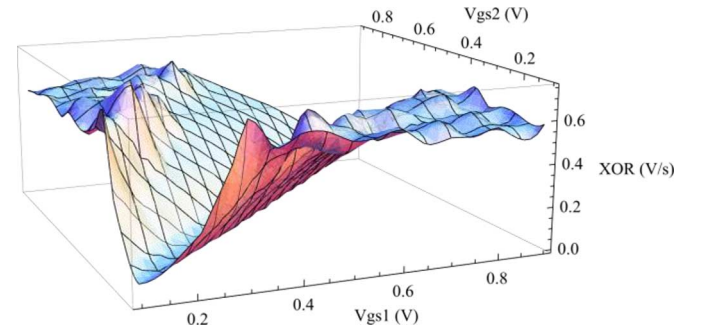


Fig. 10. XOR output as a function of  $v_{gs1}$  and  $v_{gs2}$ . Surface of the plot resembles a parabola or some even power of  $(v_{gs1} - v_{gs2})$  in the locking range and settles to a value around 0.5 outside the locking region.

time instant and finally averaging this XOR output over some time duration. The averaged XOR output for various  $v_{gs}$  values is shown in Fig. 10. We can make the following observations from it.

- It has the least value when  $v_{gs1} = v_{gs2}$ .
- Within the locking range, it rises as an even function of  $(v_{gs1} - v_{gs2})$  resembling a parabola.
- Outside the locking range, it averages to about 0.5.
- The selectivity is better at lower  $v_{gs}$  values and the XOR output becomes less selective as  $v_{gs}$  values increase.

These characteristics of the curve can be explained by realizing that the averaged XOR measure by construction is equal to the fraction of the time the system spends in the grey region (region where XOR output is 1—determined by the thresholds on  $v_1$  and  $v_2$ ) in steady state (Fig. 11). It can be seen that the XOR measure should have least value in the symmetric case when the

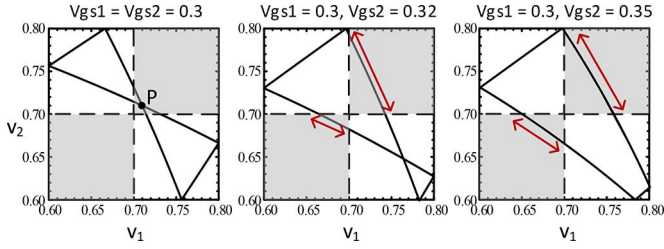


Fig. 11. Plots showing the relation between XOR output and the steady state periodic orbit of the system. XOR operation at a time instant is 1 in the grey region determined by the thresholds on respective voltages. Averaged XOR output is equal to the fraction of time spent by the system in the grey regions. XOR output is minimum in case of a butterfly shaped orbit and should increase as the orbit transitions to a rectangular orbit.

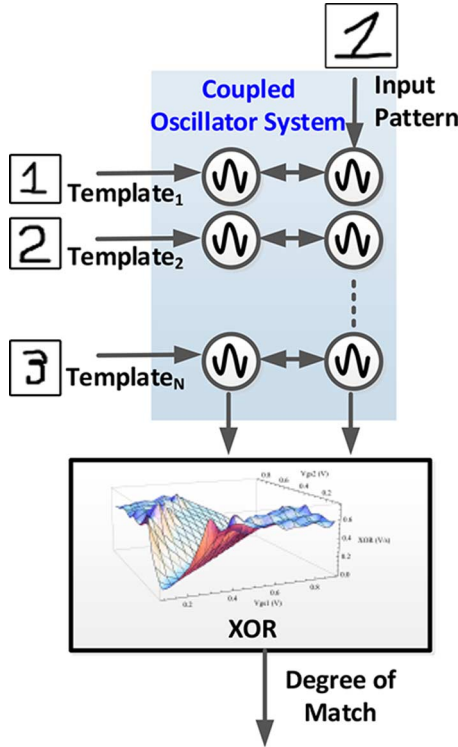


Fig. 12. Flowchart for a system using coupled oscillators and XOR output for template matching.

system locks out-of-phase and should increase as  $v_{gs}$  values diverge. The thresholds on  $v_1$  and  $v_2$  can be chosen corresponding to point P which gives 0 XOR measure in the symmetric case. Also the XOR output averages to around 0.5 outside the locking region as the system does not lock and the trajectories visit the grey and white regions almost equally. The variation in the XOR output results from the fact that the XOR measure is not time-invariant like the rotation number, its value is expected to change randomly with time and not converge.

A time domain interpretation can also be given for explaining the nature of the XOR surface of Fig. 10. The XOR operation can also be considered to measure the phase difference between the oscillators, and according to the arguments before, the system locks out-of-phase when the gate voltages are equal, and hence XOR value is minimum in this case. Also the XOR output should increase as the phase difference reduces when  $v_{gs}$  values diverge.

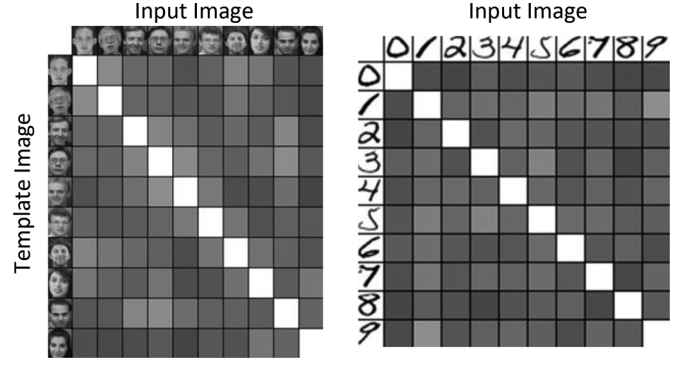


Fig. 13. XOR outputs for comparing faces (left) and handwritten number patterns (right) to stored template patterns using arrays of coupled  $VO_2$  oscillators. Grey shade corresponds to fraction of pixels with positive match, white being the highest.

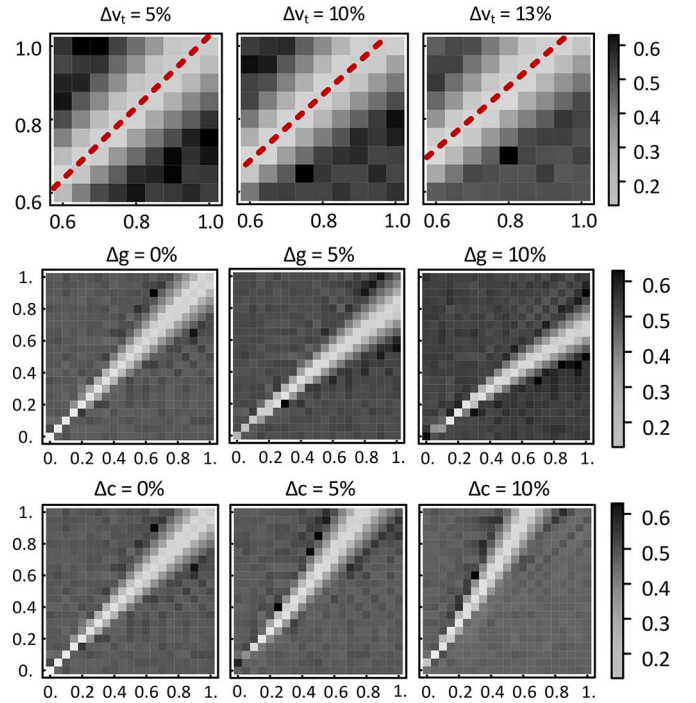


Fig. 14. XOR output as a function of  $v_{gs}$  values and its sensitivity to mismatch in  $v_t$  of the series transistor (top), MIT device conductance  $g$  (middle) and MIT device internal capacitance  $c$  (bottom). XOR output is much more susceptible to device parameters and for higher values of  $v_{gs}$ .

Such comparators would have many advantages. Firstly, they would be noise tolerant as they work on fixed-point dynamics. Secondly, their compact size would enable building of arrays of such comparators which can be used in parallel neural-like computing architectures.

## VIII. APPLICATION: TEMPLATE MATCHING

Arrays of such comparators can be used for template matching applications where element-wise comparisons suffice to decide a match. We demonstrate this by comparing images of faces and handwritten numbers. We first use the XOR measure for each pixel and calculate the number of pixels with XOR output below a threshold value  $v_{thXOR}$ . Fig. 13 shows the results of comparing faces with a relaxation comparator, where the grey shade corresponds to the fraction of pixels with

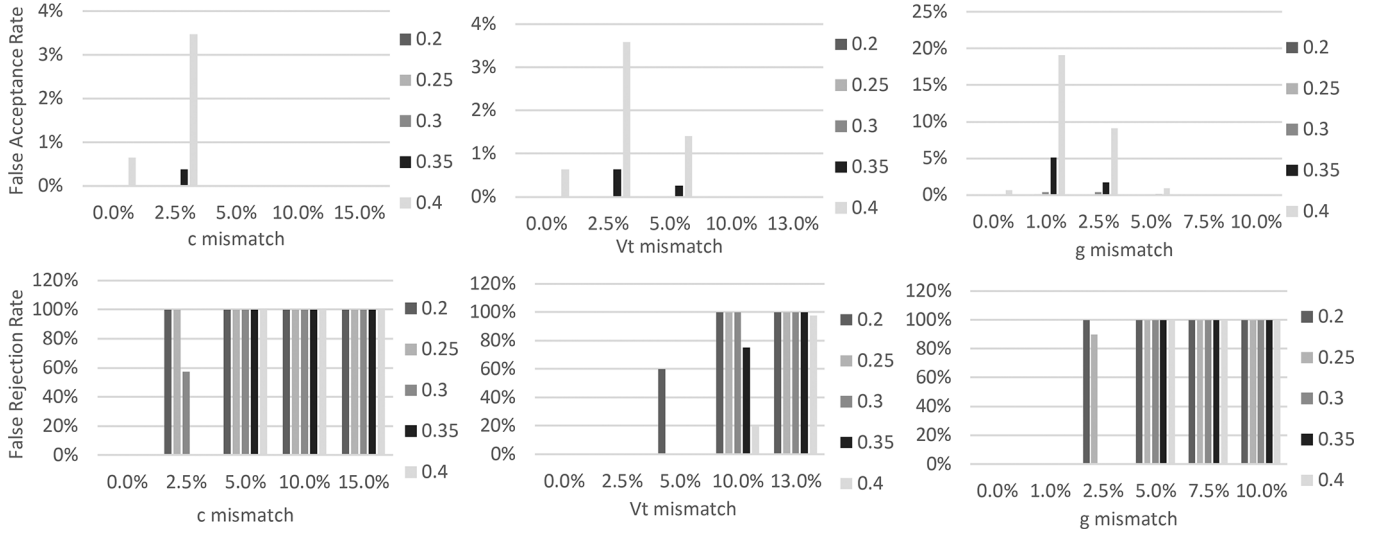


Fig. 15. False accepts (above) and False rejects (below) for varying degrees of mismatches in device internal capacitance— $c$  (left), threshold voltage  $v_t$  (middle) and device conductance in metallic state (right) for various XOR thresholds— $v_{thXOR}$ .

positive match, white being the highest. Such system followed by a winner-take-all (WTA), i.e., a threshold on the number of pixels that give a positive match, can be used to decide if the input image matches a stored template pattern. The value of  $v_{thXOR}$  is chosen around 0.2 considering the minimum values of the XOR surface in the operating range of  $v_{gs}$  values. The two thresholds described above depend on different factors. The threshold of the number of pixels for WTA would depend on the database and the error statistics required or estimated. On the other hand,  $v_{thXOR}$  would be decided more by the nature of the XOR surface (Fig. 10) and its minimum values.

A coupled  $VO_2$ -MOSFET configuration cascaded with a XOR provides a way of measuring a form of fractional distance using FSK. In this paper, we demonstrate, through measurements of individual devices and simulations of coupled oscillators, the applicability of such pairwise coupled systems in template matching. Such concepts may be extended to fully connected networks of oscillators, which have been shown to provide the basis of associative computation [1], [2]. Such associative networks can be used in more complex pattern matching and classification problems with potentially large benefits in energy efficiency [5]–[8].

## IX. VARIATION ANALYSIS

As the XOR measure is a dc measure and because the system has fixed point dynamics, temporal noise should not affect the steady state output. Hence, we restrict ourselves to variations in the form of mismatches in the device parameters  $c$ ,  $g$  of the MIT devices and  $v_t$  of the series transistors. Fig. 14 shows the effect of parametric mismatches on the XOR output. The coupled system is much more sensitive to the device parameters—internal capacitance  $c$  and metallic phase conductance  $g$ , than the threshold voltage  $v_t$  of the series transistor. Value of  $v_t$  is varied around 0.3, normalized to  $v_{dd}$ . Also the effect of mismatches is more for higher  $v_{gs}$  values, which implies that deciding the operating  $v_{gs}$  range, apart from operating in the saturation region,

will also be a trade-off in terms of combatting parametric mismatches. Larger overdrive voltages would reduce the effect of  $v_t$  variation, but would be more affected by the variations in the MIT device parameters.

Further, the effect of these parametric mismatches on template matching is analyzed. We fix 80% as the threshold for a winning match, i.e., image comparisons where 80% or more pixels give a positive match are declared matching images. Figs. 15 shows the effect of parametric mismatches on comparing images of 40 faces from the ORL database for various values of the XOR threshold  $v_{thXOR}$ . False accepts are the cases where the system gives a positive match for nonmatching images and false rejects are the cases system gives a negative match for matching images. Due to the variations, the system becomes more likely to give negative match for both matching and nonmatching images, and hence false accepts decrease and false rejects increase with the degree of mismatches.  $v_{thXOR}$  can be tuned to get desired error rates but no definite choice reduces both kinds of errors. Results are much more sensitive to variations in device parameters— $c$ ,  $g$  as compared to the  $v_t$  mismatch of the transistors.

## X. SCALABILITY ANALYSIS AND COMPARISON WITH DIGITAL LOGIC TECHNOLOGIES

For any new technology evaluation, it is important to evaluate its dimensional scalability. The  $VO_2$  device undergoes an insulating-to-metallic phase transition around a constant electric field of about  $6 \times 10^4$  V/cm. Hence, as the dimensions of the material scale, the corresponding voltage required to activate the transition will also scale thereby enabling overall voltage scaling for the system. Further, the frequency of operation is expected to increase with scaling as the intrinsic and parasitic capacitances are expected to scale faster than the charging and the discharging resistances. Fig. 16 illustrates the estimated power and frequency scaling of a pair of coupled  $VO_2$  nano-pillars as a function of their lateral dimension. Here, the  $VO_2$  nano-pillar is assumed to be 30 nm tall with a circular cross-section



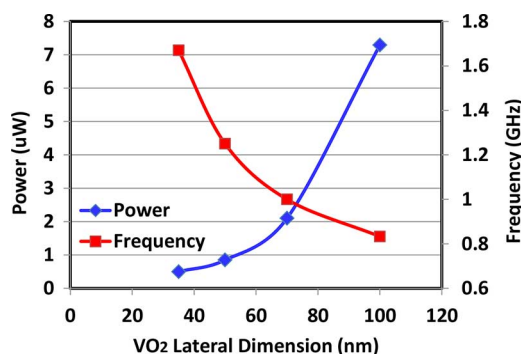


Fig. 16. Estimated power and frequency scaling of a pair of coupled VO2 nanopillars as a function of their lateral dimension.

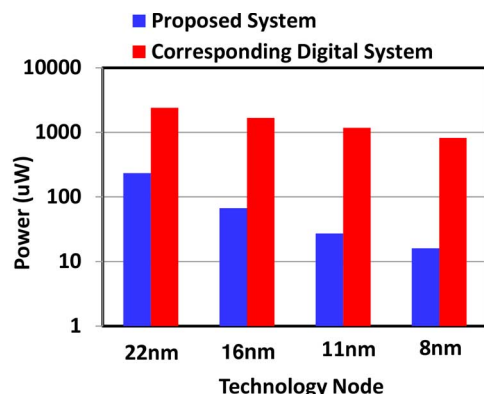


Fig. 17. Power comparison of the proposed system and the corresponding digital system for various technology nodes.

that can be potentially integrated in the metal stack on top of the series transistor. It can be seen that for GHz of operation  $\mu$ W of power consumption is expected, which is several times lower than any oscillators that can be realized using CMOS technology or novel technologies like spin-torque-oscillators. Considering a template-matching application where a  $16 \times 16$  image is scanned row-wise and a match is performed, we can estimate the power consumption in the proposed system and a corresponding digital system where an ADC converts pixel values to 8b digital words and a match is performed in the digital domain by calculating the Euclidean distance between the input and a corresponding template. We note an order of magnitude improvement in power consumption for equivalent system bandwidth for the proposed system. This illustrates the potential of such dynamical systems to perform useful computation in terms of both scalability and energy—efficiency over corresponding digital systems.

## XI. CONCLUSION

We demonstrate the possibility of utilizing the coupling dynamics of VO<sub>2</sub> based relaxation oscillators and present a mathematical framework for modeling the experimentally verified dynamics of such a system. Using an XOR measure to capture the position of fixed-point in a coupled system of two oscillators with nonidentical native frequencies, we demonstrate possible application of this computing fabric in template matching. Variation analysis on such systems exhibits strong sensitivity to

parametric variations and calls for further work on matching, parameter control and robust design methodologies for large-scale systems.

## ACKNOWLEDGMENT

The authors would like to thank Dr. H. Paik and Prof. D. G. Schlom at Cornell University for growing the epitaxial VO<sub>2</sub> films, and Prof. V. Narayanan at The Pennsylvania State University for helpful discussions.

## REFERENCES

- [1] E. M. Izhikevich, Computing with oscillators 2000 [Online]. Available: <http://citeseerx.ist.psu.edu/viewdoc/summary?doi=10.1.1.33.1937>
- [2] D. E. Nikonov, G. Csaba, W. Porod, T. Shibata, D. Voils, D. Hammerstrom, I. A. Young, and G. I. Bourianoff, Coupled-oscillator associative memory array operation arXiv e-print 1304.6125, Apr. 2013.
- [3] F. C. Hoppensteadt and E. M. Izhikevich, "Oscillatory neurocomputers with dynamic connectivity," *Phys. Rev. Lett.*, vol. 82, no. 14, pp. 2983–2986, Apr. 1999.
- [4] N. Vijaykrishnan, S. Datta, G. Cauwenberghs, D. Chiarulli, S. Levitan, and P. Wong, "Video analytics using beyond CMOS devices," in *Proc. IEEE Design, Automat. Test Eur. Conf. Exhibit.*, Mar. 2014, pp. 1–5.
- [5] T. Roska, A. Horvath, A. Stubendek, F. Corinto, G. Csaba, W. Porod, T. Shibata, and G. Bourianoff, "An associative memory with oscillatory CNN arrays using spin torque oscillator cells and spin-wave interactions architecture and end-to-end simulator," in *Proc. 13th Int. Workshop Cellular Nanoscale Netw. Appl.*, 2012, pp. 1–3.
- [6] T. Shibata, R. Zhang, S. P. Levitan, D. E. Nikonov, and G. I. Bourianoff, "CMOS supporting circuitries for nano-oscillator-based associative memories," in *Proc. 13th Int. Workshop Cellular Nanoscale Netw. Appl.*, 2012, pp. 1–5.
- [7] S. P. Levitan, Y. Fang, D. H. Dash, T. Shibata, D. E. Nikonov, and G. I. Bourianoff, "Non-Boolean associative architectures based on nano-oscillators," in *Proc. 13th Int. Workshop Cellular Nanoscale Netw. Appl.*, 2012, pp. 1–6.
- [8] G. Csaba, M. Pufall, D. E. Nikonov, G. I. Bourianoff, A. Horvath, T. Roska, and W. Porod, "Spin torque oscillator models for applications in associative memories," in *Proc. 13th Int. Workshop Cellular Nanoscale Netw. Appl.*, 2012, pp. 1–2.
- [9] M. Sharad, K. Yogendra, and K. Roy, "Dual pillar spin torque nano-oscillator," *Appl. Phys. Lett.*, vol. 103, no. 15, pp. 152403–152403-5, Oct. 2013.
- [10] F. J. Morin, B. T. Laboratories, and M. Hill, "Oxides which show a metal-to-insulator transition at the Neel temperature," *Phys. Rev. Lett.*, vol. 3, no. 1, pp. 34–36, Jul. 1959.
- [11] R. A. Fastnacht, S. Jin, T. H. Tiefel, M. McCormack, R. Ramesh, and L. H. Chen, "Thousandfold change in resistivity in magnetoresistive La-Ca-Mn-O films," *Science*, vol. 264, no. 5157, pp. 413–415, Apr. 1994.
- [12] M. Imada, A. Fujimori, and Y. Tokura, "Metal-insulator transitions," *Rev. Mod. Phys.*, vol. 70, no. 4, pp. 1039–1263, Oct. 1998.
- [13] Bednorz, J. George, and K. A. Müller, "Possible highT<sub>c</sub> superconductivity in the Ba<sup>2+</sup> La<sup>2+</sup> Cu<sup>2+</sup> O system," *Zeitschrift für Physik B Condensed Matter*, vol. 64, no. 2, pp. 189–193, 1986.
- [14] L. A. Ladd and W. Paul, "Optical and transport properties of high quality crystals of V<sub>2</sub>O<sub>4</sub> near the metallic transition temperature," *Solid State Commun.*, vol. 7, no. 4, pp. 425–428, Feb. 1969.
- [15] M. Nakano, K. Shibuya, D. Okuyama, T. Hatano, S. Ono, M. Kawasaki, Y. Iwasa, and Y. Tokura, "Collective bulk carrier delocalization driven by electrostatic surface charge accumulation," *Nature*, vol. 487, no. 7408, pp. 459–462, Jul. 2012.
- [16] E. Strelcov, Y. Lilach, and A. Kolmakov, "Gas sensor based on metal-insulator transition in VO<sub>2</sub> nanowire thermistor," *Nano Lett.*, vol. 9, no. 6, pp. 2322–2326, Jun. 2009.
- [17] M. M. Qazilbash, M. Brehm, B.-G. Chae, P.-C. Ho, G. O. Andreev, B.-J. Kim, S. J. Yun, A. V. Balatsky, M. B. Maple, F. Keilmann, H.-T. Kim, and D. N. Basov, "Mott transition in VO<sub>2</sub> revealed by infrared spectroscopy and nano-imaging," *Science*, vol. 318, no. 5857, pp. 1750–1753, Dec. 2007.
- [18] B.-J. Kim, Y. Lee, S. Choi, J.-W. Lim, S. Yun, H.-T. Kim, T.-J. Shin, and H.-S. Yun, "Micrometer x-ray diffraction study of VO<sub>2</sub> films: Separation between metal-insulator transition and structural phase transition," *Phys. Rev. B*, vol. 77, no. 23, p. 235401, Jun. 2008.

- [19] H.-T. Kim, B.-G. Chae, D.-H. Youn, S.-L. Maeng, G. Kim, K.-Y. Kang, and Y.-S. Lim, "Mechanism and observation of Mott transition in VO<sub>2</sub>-based two- and three-terminal devices," *New J. Phys.*, vol. 6, pp. 52–52, May 2004.
- [20] A. Cavalleri, T. Dekorsy, H. Chong, J. Kieffer, and R. Schoenlein, "Evidence for a structurally-driven insulator-to-metal transition in VO<sub>2</sub>: A view from the ultrafast timescale," *Phys. Rev. B*, vol. 70, no. 16, p. 161102, Oct. 2004.
- [21] J. Cao, E. Ertekin, V. Srinivasan, W. Fan, S. Huang, H. Zheng, J. W. L. Yim, D. R. Khanal, D. F. Ogletree, J. C. Grossman, and J. Wu, "Strain engineering and one-dimensional organization of metal-insulator domains in single-crystal vanadium dioxide beams," *Nat. Nanotechnol.*, vol. 4, no. 11, pp. 732–737, Nov. 2009.
- [22] J. W. Tashman, J. H. Lee, H. Paik, J. A. Moyer, R. Misra, J. A. Mundy, T. Spila, T. A. Merz, J. Schubert, D. A. Muller, P. Schiffer, and D. G. Schlom, "Epitaxial growth of VO<sub>2</sub> by periodic annealing," *Appl. Phys. Lett.*, vol. 104, no. 6, p. 063104, Feb. 2014.
- [23] A. Kar, N. Shukla, E. Freeman, H. Paik, H. Liu, R. Engel-Herbert, S. S. N. Bharadwaja, D. G. Schlom, and S. Datta, "Intrinsic electronic switching time in ultrathin epitaxial vanadium dioxide thin film," *Appl. Phys. Lett.*, vol. 102, no. 7, p. 072106, 2013.
- [24] M. D. Pickett and R. S. Williams, "Sub-100 fJ and sub-nanosecond thermally driven threshold switching in niobium oxide crosspoint nanodevices," *Nanotechnology*, vol. 23, no. 21, p. 215202, June 2012.
- [25] S. Kaka, M. R. Pufall, W. H. Rippard, T. J. Silva, S. E. Russek, and J. A. Katine, "Mutual phase-locking of microwave spin torque nano-oscillators," *Nature*, vol. 437, no. 7057, pp. 389–392, Sept. 2005.
- [26] H. Eisele, "State of the art and future of electronic sources at terahertz frequencies," *Electron. Lett.*, vol. 46, no. 26, p. S8, 2010.
- [27] F. C. Hoppensteadt and E. M. Izhikevich, "Pattern recognition via synchronization in phase-locked loop neural networks," *IEEE Trans. Neural Netw.*, vol. 11, no. 3, pp. 734–738, May 2000.
- [28] T. J. Silva and W. H. Rippard, "Developments in nano-oscillators based upon spin-transfer point-contact devices," *J. Magnetism Magnetic Mater.*, vol. 320, no. 7, pp. 1260–1271, Apr. 2008.
- [29] T. Saito, "On a coupled relaxation oscillator," *IEEE Trans. Circuits Syst.*, vol. 35, no. 9, pp. 1147–1155, Sep. 1988.
- [30] C.-L. Hu, "Self-sustained oscillation in an R<sub>H</sub>-C or R<sub>H</sub>-L circuit containing a hysteresis resistor R<sub>H</sub>," *IEEE Trans. Circuits Syst.*, vol. 33, no. 6, pp. 636–641, 1986.
- [31] S. H. Strogatz, "From Kuramoto to Crawford: Exploring the onset of synchronization in populations of coupled oscillators," *Physica D: Nonlinear Phenomena*, vol. 143, no. 1, pp. 1–20, 2000.
- [32] Database of faces [Online]. Available: <https://www.cl.cam.ac.uk/research/dtg/attarchive/facedatabase.html>
- [33] The MNIST Database of Handwritten Digits [Online]. Available: <http://yann.lecun.com/exdb/mnist/>



**Abhinav Parihar** received the B.Tech. degree in electrical engineering from Indian Institute of Technology Delhi, New Delhi, India, in 2012. He is currently working toward the Ph.D. degree at the School of Electrical and Computer Engineering, Georgia Institute of Technology, Atlanta, GA, USA.



**Nikhil Shukla** received the B.S. degree in electronics and telecommunications engineering from the University of Mumbai, Mumbai, India, in 2010. He is currently working toward the Ph.D. degree in electrical engineering in the Department of Electrical Engineering, Pennsylvania State University, University Park, PA, USA.



**Suman Datta** (F'13) received the B.S. degree in electrical engineering from the Indian Institute of Technology, Kanpur, India, in 1995, and the Ph.D. degree in electrical and computer engineering from the University of Cincinnati, Cincinnati, OH, USA, in 1999.

From 1999 to 2007, he was a member of the Logic Technology Development Group, Intel Corporation. He was instrumental in the demonstration of III-V quantum-well transistors operating at room temperature with a record energy delay product, the first experimental demonstration of high-performance high- $\kappa$ /metal gate CMOS transistors, and the invention and demonstration nonplanar "trigate transistors." In 2007, he was the Joseph Monkowski Associate Professor of Electrical Engineering with Pennsylvania State University, University Park, PA, USA, where he is currently a Professor of Electrical Engineering. He is the holder of more than 160 U.S. patents. His group is exploring new materials and novel device architecture for CMOS enhancement and replacement for future energy-efficient computing applications.

Dr. Datta is a Distinguished Lecturer of the IEEE Electron Devices Society.



**Arijit Raychowdhury** (M'07–SM'13) received the B.E. degree in electrical and telecommunication engineering from Jadavpur University, Kolkata, India, and the Ph.D. degree in electrical and computer engineering from Purdue University, West Lafayette, IN, USA.

He is currently an Associate Professor in the School of Electrical and Computer Engineering, Georgia Institute of Technology, Atlanta, GA, USA, where he joined in January, 2013. His industry experience includes five years as a Staff Scientist in

the Circuits Research Lab, Intel Corporation and a year as an Analog Circuit Designer with Texas Instruments Inc. His research interests include digital and mixed-signal circuit design, design of on-chip sensors, memory, and device-circuit interactions. He holds more than 25 U.S. and international patents and has published over 100 articles in journals and refereed conferences.

Dr. Raychowdhury is the winner of the Intel Labs Technical Contribution Award, 2011; Dimitris N. Chorafas Award for outstanding doctoral research, 2007; the Best Thesis Award, College of Engineering, Purdue University, 2007; Best Paper Awards at the International Symposium on Low Power Electronic Design (ISLPED) 2012, 2006; IEEE Nanotechnology Conference, 2003; SRC Technical Excellence Award, 2005; Intel Foundation Fellowship 2006, NASA INAC Fellowship 2004, and the Meissner Fellowship 2002.